Ionics (2022) 28:4149–4158
https://doi.org/10.1007/s11581-022-04645-w

ORIGINAL PAPER

Novel metal organic frameworks derived nitrogen-doped porous carbon-covered Co_3O_4 nanoparticle composites as anode materials for efficient lithium storage

Zhipeng Yang[1] · Xiudong Chen[1,2] · Ping Yan[1] · Changchao Zhan[1] · Yawei Wang[1] · Jin-Hang Liu[1]

Received: 21 March 2022 / Revised: 12 May 2022 / Accepted: 11 June 2022 / Published online: 20 June 2022

Abstract

Metal-organic frameworks (MOFs) with porous structures derived from transition metal oxides have been shown to be effective at storing lithium and converting it. During the course of this research, N-doped porous carbon-covered Co_3O_4 nanoparticle composites (Co_3O_4/NC-2) were manufactured by employing a novel cobalt-based MOF as a sacrificial template. The N-doped porous carbon coating improves the electrical conductivity while also reducing the path that Li^+ takes to diffuse through the material. During this time, the composite's volume change that occurs during galvanostatic discharge/charge cycles is effectively buffered, and the cycling stability of the composite is improved. As a result, Co_3O_4/NC-2 has excellent lithium storage properties. After 100 cycles at 0.1 A g^{-1}, the reversible capacity of Co_3O_4/NC-2 is 884.2 mAh g^{-1}. Furthermore, Co_3O_4/NC-2 has an excellent rate capability. The reversible specific capacity can be recovered to 1124.6 mAh g^{-1} by increasing the current density from 0.1 A g^{-1} to 5 A g^{-1} and back to 0.1 A g^{-1}. We design and synthesize a novel MOF as a sacrificial template in this paper to provide a simple method for fabricating highly electrochemical electrode materials.

Keywords Metal-organic frameworks · Lithium ion batteries · Anode materials · Nitrogen-doped porous carbon · Nanoparticles

Introduction

The problem of increasing energy demand around the world has become more serious as a direct result of the rapid development of industry. In an effort to mitigate the damage caused by the depletion of fossil fuels and the environmental problems that this entails, researchers have investigated the feasibility of generating electricity from renewable energy sources such as hydro, solar, and wind power. Researchers have developed and implemented environmentally friendly technologies for efficient electrochemical energy storage and conversion in order to increase the availability of energy sources in a timely manner and improve their reliability [1]. The most developed forms of energy storage are lithium-ion batteries, which have a high reversible capacity and do not suffer from the memory effect [2–4]. However, the theoretical power of commercial graphite anode materials is only 372 mAh g^{-1}, which means that it is not capable of meeting the growing demand for applications that involve energy storage [5–7]. As a result, the development of high-performance materials for the anode of lithium-ion batteries has become an active area of research. As a result of the high theoretical capacity of transition metal oxides, a great number of research groups have started concentrating their efforts on the development of transition metal oxides with a variety of morphologies and pore sizes for use as anode materials in LIBs [8–10]. In particular, composite electrode materials with long-cycle stability are obtained by compounding with carbon materials and doping heteroatoms [11–18]. Nevertheless, some challenges remain in synthesizing metal oxide electrodes with high electrical conductivity and structural stability.

✉ Xiudong Chen
chenxiudong_@126.com

✉ Jin-Hang Liu
ljh2016HUST@126.com

[1] School of Chemistry and Chemical Engineering, Jiangxi Province Engineering Research Center of Ecological Chemical Industry, Jiujiang University, Jiujiang 332005, Jiangxi, China

[2] State Key Laboratory of Organic-Inorganic Composites, Beijing University of Chemical Technology, Beijing 100029, China

Porous crystalline materials known as metal-organic frameworks (MOFs) have periodic network structures that are formed by the self-assembly of transition metal ions and organic ligands [19]. More and more research groups are paying attention to specific MOFs because of the high specific surface area, the tunable pore structure, and the versatility of MOFs [20–22]. The direct use of MOFs as electrode materials, on the other hand, continues to be plagued by issues such as a lack of adequate electrical conductivity. However, the derived materials that are obtained by annealing MOFs at high temperatures inherit their advantages, which include a large specific surface area and a high porosity. These materials are widely used as anode materials for LIBs [23]. Because of the high porosity, lithium-ion diffusion is made easier, and kinetics are improved. Because of the framework's large specific surface area and the even distribution of active materials across its surface, there are many reaction sites available for redox reactions. In addition, the stable structure of MOFs-derived materials has the ability to provide sufficient space to buffer the volume expansion that occurs during cycling. This helps to prevent the pulverization of the electrode material and its dissolution in the electrolyte, which ultimately leads to an improvement in the cycling stability. For instance, Wang et al. used a straightforward heat treatment to obtain Fe_2O_3@C core@shell anode material, which they demonstrated to have excellent cycling stability [24].

Herein, a novel precursor known as Co-MOF was produced using the hydrothermal method and then annealed to produce N-doped porous carbon-covered Co_3O_4 nanoparticle composites (Co_3O_4/NC-2). Co_3O_4/NC-2, when utilized as an anode material for lithium-ion batteries, demonstrated both a high reversible specific capacity (884.2 mAh g^{-1} after 100 cycles at 0.1 A g^{-1}) and excellent rate performance (646.4 mAh g^{-1} at 2 A g^{-1}). The excellent electrochemical performance can primarily be attributed to the synergistic effect that the various components have on one another as well as the stable nanoporous structure. Because of the nanoporous structure's ability to increase the contact area between the electrode and the electrolyte and to shorten the paths that ions and electrons take as they diffuse through the material [25, 26], a rapid transfer of charges can be ensured. During the subsequent high-temperature carbonization process, the N atoms that are carried by the 4-cyanobenzoic acid organic ligand are able to be uniformly distributed in the Co_3O_4/NC-2 nanocomposite. This opens up a new avenue for the application of this novel organic ligand. As a result, there is a good possibility that Co_3O_4/NC-2 will find use in the future as an anode material for high-performance lithium storage.

Experimental section

Materials

$LiPF_6$ electrolyte (1 M in the mixed ethylene carbonate/diethyl carbonate solution, 1:1, w/w) was brought from Do Do Chem. The other reagents and chemicals were from Sinopharm Chemical Reagent Co., Ltd. (Shanghai, China). All the chemicals were utilized in their received status without further purification.

Material synthesis

In a typical synthesis process, 0.5238 g $Co(NO_3)_2{\cdot}6H_2O$ and 0.2942 g $C_8H_5NO_2$ (4-cyanobenzoic acid) were dissolved in 10 mL DMF at room temperature, respectively. Then, slowly drop the $Co(NO_3)_2{\cdot}6H_2O$ solution into the 4-cyanobenzoic acid solution, and continue stirring for 20 min to obtain a mixed solution. The mixed solution was transferred into a 50 mL Teflon-lined stainless steel autoclave and kept at 180 °C for 12 h. After cooling to room temperature, the solid product was collected through centrifugation, washed with deionized water and ethanol several times, and then dried at 60 °C. The dried solid was ground into powder in an agate mortar to obtain the primary product, denoted as Co-MOF. The prepared Co-MOF was poured into a porcelain boat and heated with a tube furnace. The Co_3O_4/NC-1 composite was obtained in an air atmosphere by heating to 500 °C at a heating rate of 2 ℃ min^{-1}, followed by calcination for 2 h. Co_3O_4/NC-2 and Co_3O_4/NC-3 were prepared by changing the above calcination temperature to 600 °C and 700 °C, respectively.

Material characterization

Transmission electron microscope (TEM) and scanning electron microscopy (SEM) characterizations were conducted by JEM-2010F and JSM-6700F, respectively, to survey the morphologies of materials. Structural information of the as-synthesized products was investigated by Powder X-ray diffractometer (PXRD, Cu Ka radiation, Rigaku D/max-2550 V), TGA (NETZSCH STA 409 PG/PC in Air), and Raman spectroscopy (Renishaw in plus, excitation wavelength: 785 nm, spot size ~ 1.2 μm, excitation power 3 mW). The Brunauer-Emmett-Teller (BET) surface area and porous structures (Micromeritics Instrument Corp, ASAP 2460 2.02, analysis adsorptive: N_2), and X-ray photoelectron spectroscopy (XPS, Thermo Fischer, ESCALAB 250Xi).

Electrochemical measurements

A uniform slurry was obtained by mixing active material (60 wt%), acetylene black (20 wt%), and poly(vinylidene

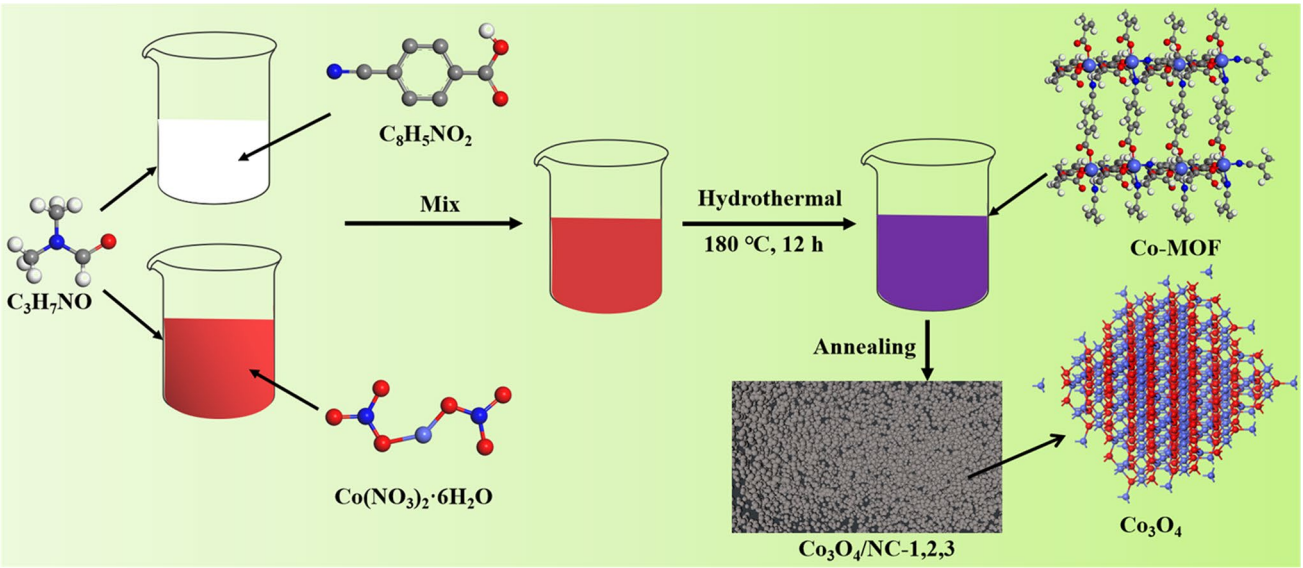

Scheme 1 Schematic illustration showing the fabrication process of the Co_3O_4/NC-1, Co_3O_4/NC-2, and Co_3O_4/NC-3 composites

fluoride) binder (PVDF, 20 wt%) in 1-methayl-2-pyrrolidinone solution. After that, the slurry was coated on copper foil and dried at 60 °C for more than 12 h in a vacuum oven. A lithium foil was sliced into disks (12 mm in diameter) and used as the counter electrode. 1 M $LiPF_6$ solution in the mixed solvent of ethylene carbonate (EC) and dimethyl carbonate (DEC) (1:1, v/v) was chosen as the electrolyte. Polyethylene membrane (Celgard-2300) has functioned as the separator.

A LAND-CT2001 test system was adopted for the galvanostatic charge-discharge tests under different current densities (voltage range 1 mV-3.0 V) and galvanostatic intermittent titration technique (GITT) measurements. CV (scan rate 0.2-1.0 mV/s) and the EIS test (frequency range 10^5-0.01 Hz) were evaluated on the CHI760E electrochemical workstation.

All the electrochemical tests were conducted at 25 °C.

Results and discussion

Scheme 1 provides a diagrammatic description of the synthesis process for the Co_3O_4/NC-1, Co_3O_4/NC-2, and Co_3O_4/NC-3 electrodes. Techniques known as scanning electron microscopy (SEM) and transmission electron microscopy (TEM) were utilized in order to investigate the microstructures of the materials. The precursor Co-MOF materials, which were manufactured through a straightforward hydrothermal process, exhibited a nanoparticle stacking structure (Fig. 1a). Co_3O_4/NC-1, Co_3O_4/NC-2, and Co_3O_4/NC-3 were produced by subjecting the precursor Co-MOF to an annealing process at temperatures of 500, 600, and 700 ℃, respectively. It is easy to see, in comparison to the precursor, that the Co_3O_4/NC-2 composites have better dispersion, more pronounced granularity, and a rich pore structure, all of which are characteristics of nanoparticles (Fig. 1b). When compared to Co_3O_4/NC-2, the Co_3O_4/NC-1 and Co_3O_4/NC-3 composites have poor electrochemical performance because they have low nanoparticle dispersion and partially disrupted systems, respectively (Fig. S1). In addition, the TEM images of Co_3O_4/NC-2 show that nanoparticles of Co_3O_4 are present, and porous carbon is wrapped around each of the nanoparticles. To effectively improve the electrical conductivity of the electrode material and to buffer the volume expansion that occurs during charging and discharging, the porous carbon layer that is located on the surface of the electrode. This helps to improve the cycling stability (Fig. 1c). The HAADF-STEM elemental mapping images are displayed in Fig. 1d–i. These images demonstrate that the elements C, N, O, and Co are uniformly distributed throughout the Co_3O_4/NC-2 nanocomposite. This suggests that the Co_3O_4 nanoparticles present in the material have good compatibility with the nitrogen-doped carbon matrix. The electrochemical cycling process of the Co_3O_4/NC-2 composite nanomaterials is significantly aided by the excellent compatibility between the two components. Detected lattice fringes with distances of 0.47 nm can be satisfactorily assigned to the (111) plane of Co_3O_4, as shown by high-resolution transmission electron microscope images in Fig. S2.

The chemical composition and structure of Co-MOF, Co_3O_4/NC-1, Co_3O_4/NC-2, and Co_3O_4/NC-3 composite were further determined by powder X-ray diffraction (PXRD), thermogravimetric analysis (TGA), N_2 adsorption and desorption curves, and X-ray photoelectron

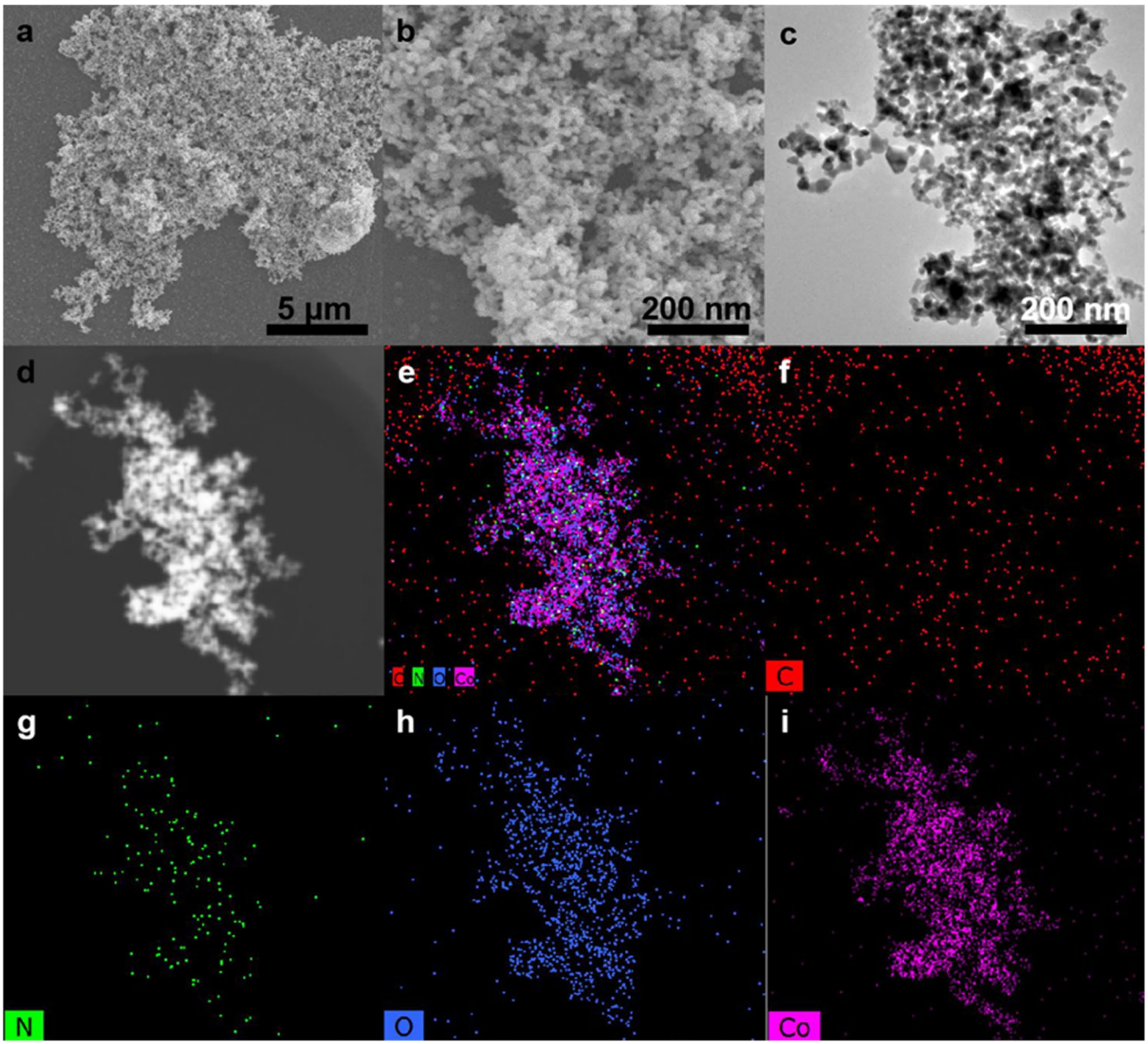

Fig. 1 **a** SEM image of Co-MOF. **b** SEM image and **c** TEM images of Co_3O_4/NC-2. **d–i** HAADF-STEM and elemental mapping images of Co_3O_4/NC-2

spectroscopy (XPS). The PXRD patterns of the prepared Co-MOF precursors have been measured, and the results show that they have a good degree of crystallinity (Fig. S3). TGA measurements were carried out in a nitrogen atmosphere from room temperature all the way up to 800 °C in order to investigate the thermal stability of the Co-MOF precursors (Fig. S4). The evaporation of crystalline water and adsorbed water accounted for the majority of the mass loss that was observed in the TGA test results when it was conducted at temperatures lower than 125 °C. At temperatures ranging from 125 to 590 °C, there was an approximate loss of mass of 28.8%. This was primarily caused by the disintegration of the skeleton and the breakdown of organic ligands. As Fig. 2a shows the XRD pattern of Co_3O_4/NC-2 composite, the characteristic peak positions of 19.0°, 31.3°, 26.8°, 38.5°, 44.8°, 59.3°, and 65.2° correspond to (111), (220), (311), (222), (400), (511), and (440) crystal planes of Co_3O_4 (JCPDS No. 43–1003), respectively [27–29], proving the formation of Co_3O_4. The XRD peaks of Co_3O_4/NC-1 and Co_3O_4/NC-3 are consistent with Co_3O_4/NC-2, indicating that the annealing temperature has no effect on the crystal structure of the material. The electrochemical properties of the material depend largely on the porosity, so N_2 adsorption-desorption isotherm measurements were performed. As shown in Fig. S5, the specific surface area of Co-MOF is 208.2 $m^2\ g^{-1}$, and the pore size distribution

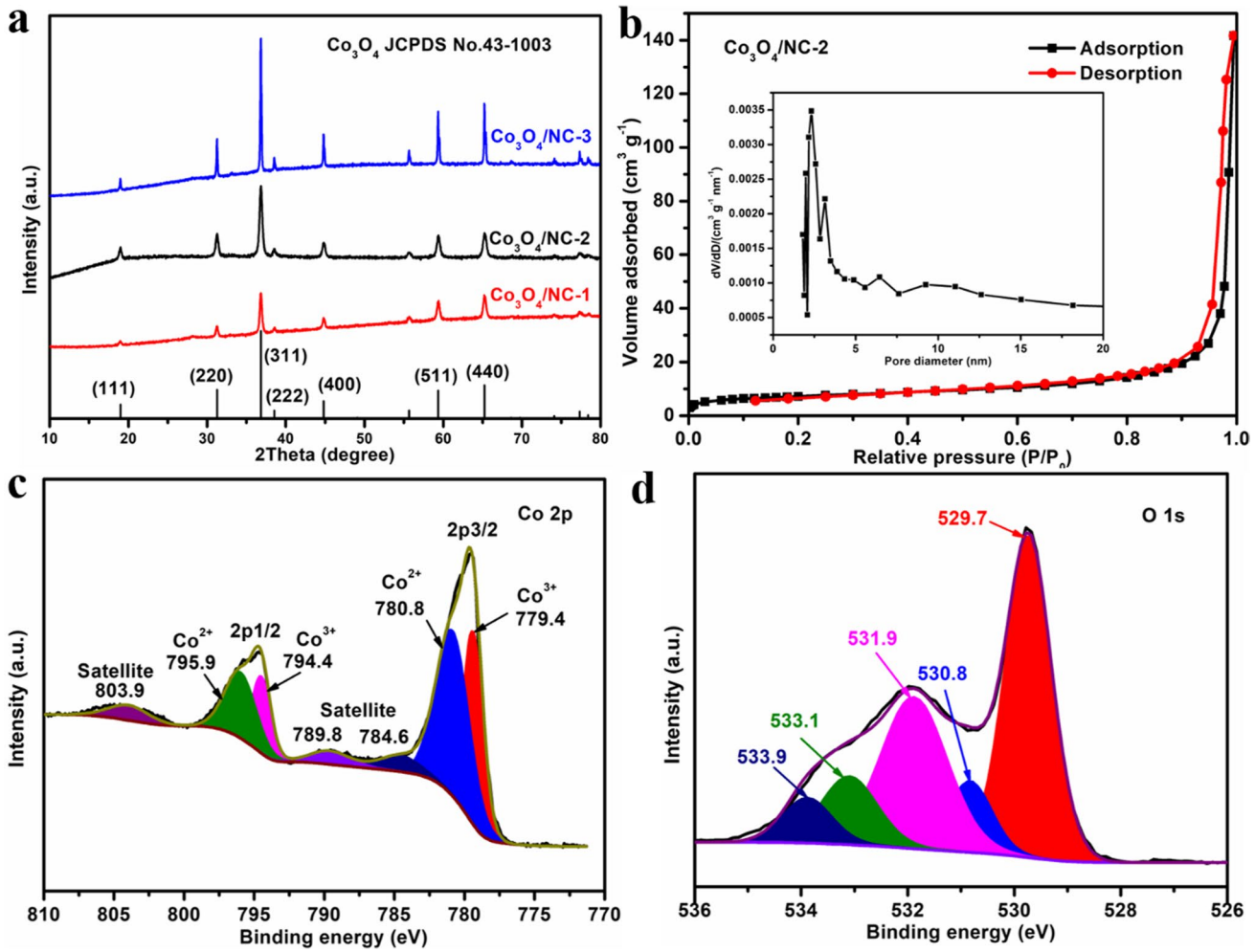

Fig. 2 **a** XRD patterns of the Co_3O_4/NC-1, Co_3O_4/NC-2, and Co_3O_4/NC-3. **b** N_2 adsorption/desorption isothermal curves of the Co_3O_4/NC-2; insert: the pore size distribution. XPS spectrum of the Co_3O_4/NC-2 composites, **c** Co 2p spectrum, **d** O 1 s spectrum

shows its mesoporous character. In contrast, the specific surface area of Co_3O_4/NC-2 obtained by high-temperature forging is only 25.0 $m^2\ g^{-1}$ and exhibits a richer pore structure, mainly attributed to the release of gases from the high-temperature cracking of organic ligands (Fig. 2b).The porous structure of Co_3O_4/NC-2 can provide a channel for the transport of lithium ions and accelerate the Li^+ transfer rate. To further determine the chemical composition of Co_3O_4/NC-2, XPS measurements were used, and the results are shown in Fig. 2c, d. It can be seen from the binding energy spectrum of Co 2p that two main peaks with electron energies of 779.7 eV and 794.8 eV appear at Co 2p3/2 and Co 2p1/2, which are typical peaks of Co_3O_4 (Fig. 2c). The peak of Co 2p3/2 can be divided into two peaks with electron energies of 779.4 eV and 780.8 eV, corresponding to Co^{3+}2p3/2 and Co^{2+}2p3/2, respectively [30]. Co 2p1/2 can also be divided into two peaks, corresponding to Co^{3+}2p1/2 at electron energy of 794.4 eV and Co^{2+} 2p1/2 at electron energy of 795.9 eV, respectively. In addition, three satellite peaks appear at 784.6 eV, 789.8 eV, and 803.9 eV. The XPS spectrum of O 1 s can be divided into five main peaks (Fig. 2d). The peaks at 529.7 eV and 530.8/531.9 eV can be assigned to the peaks of lattice oxygen in the Co_3O_4/NC-2 composite and the corresponding peaks of crystal surface OH, respectively. The peaks at 533.1 eV and 533.9 eV can be assigned to the oxygen peaks of H_2O on the crystal surface and the oxygen peaks of defect sites in the Co_3O_4/NC-2 composite, respectively. The XPS analysis of the Co_3O_4/NC-2 composite further proves that the main composition of the material is Co_3O_4.

The Co_3O_4/NC-1, Co_3O_4/NC-2, and Co_3O_4/NC-3 composites were subjected to cyclic voltammetry testing in order to conduct an in-depth investigation. The CV curves of Co_3O_4/NC-2 for the first 3 cycles at 0.1 mV s^{-1} with a discharge window of 0.001-3 V are depicted in Fig. 3a. There is a distinct reduction peak at the first circle at 0.88 V, which corresponds to the reduction of Co_3O_4 to Co and the formation of SEI film. This can be seen by looking at the graph.

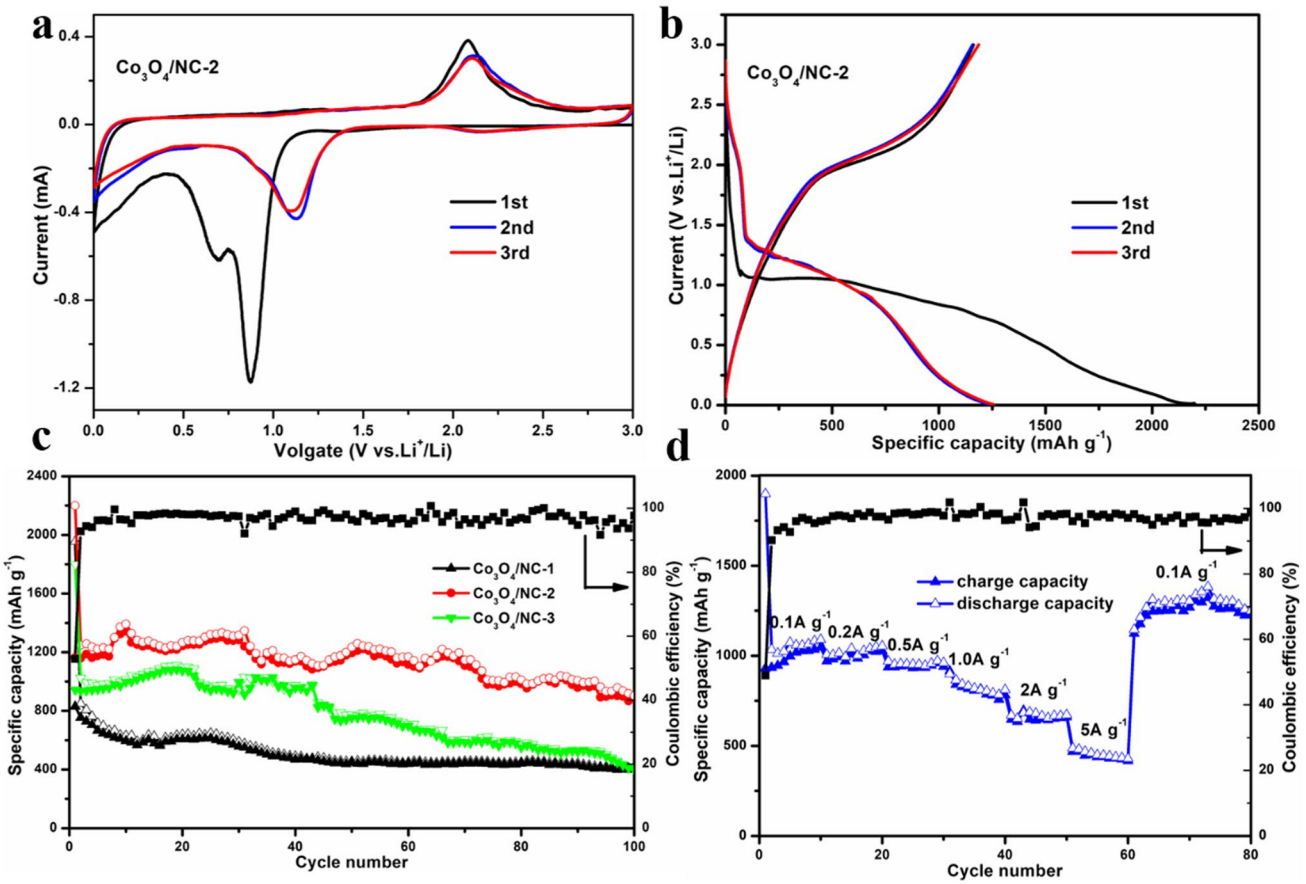

Fig. 3 **a** The CV curves of Co_3O_4/NC-2 at 0.1 mV s^{-1}. **b** Charge-discharge curves of Co_3O_4/NC-2 for the first 3 cycles at 0.1 A g^{-1}. **c** Cycle performances of Co_3O_4/NC-1, Co_3O_4/NC-2, and Co_3O_4/NC-3 at 0.1 A g^{-1}. **d** rate capability tests at various current densities (0.1-5 A $g.^{-1}$) of the Co_3O_4/NC-2

After that, there is a distinct reduction peak located close to the 2.08 V oxidation peak, and this can be attributed to the reversible reoxidation of cobalt metal to Co^{2+} and Co^{3+} [31–33]. Additionally, the reduction peak moves to 1.12 V in the two subsequent cycles, while the position of the oxidation peak remains essentially unchanged, indicating the good electrochemical reversibility of the Co_3O_4/NC-2 composite [34]. This is demonstrated by the fact that the position of the oxidation peak remains essentially unchanged. It can be deduced from the fact that the redox peaks in the CV curves of Co_3O_4/NC-1 and Co_3O_4/NC-3 are identical to those of Co_3O_4/NC-2 that these substances share the same reaction mechanism (Fig. S6). The charge and discharge curves for Co_3O_4/NC-2 are shown in Fig. 3b, and they reveal a prominent voltage plateau at 1.1 V in the initial discharge curve. This plateau corresponds to the lithiation reaction and the reduction of Co_3O_4 and can be seen in the initial discharge curve. Additionally, the plateau of the charging curve occurs at approximately 1.9 V, which corresponds to the de-lithiation of Li_2O and the oxidation of Co. This position coincides with the peak position in the CV curve [34]. The charge/discharge curves of Co_3O_4/NC-1 and Co_3O_4/NC-3, respectively (Fig. S7). These curves have the same charging and discharging plateaus as those of Co_3O_4/NC-2, which once again indicates that the charging and discharging mechanism is the same.

At a current density of 0.1 A g^{-1} and a voltage range of 0.001-3.0 V, the cycling curves of Co_3O_4/NC-1, Co_3O_4/NC-2, and Co_3O_4/NC-3 were evaluated (Fig. 3c). Co_3O_4/NC-1, Co_3O_4/NC-2, and Co_3O_4/NC-3 each exhibit good initial reversible specific capacities of 830.2 mAh g^{-1}, 1162.4 mAh g^{-1}, and 944.3 mAh g^{-1}, respectively, because of their distinctive nanostructures. However, the first cycle Coulombic efficiencies of Co_3O_4/NC-1, Co_3O_4/NC-2, and Co_3O_4/NC-3 were 42.4%, 52.9%, and 52.5%, respectively. In the subsequent charge-discharge cycles, these efficiencies quickly approached 100%. The formation of an SEI film and the decomposition process of the electrolyte are primarily to blame for the low Coulombic efficiency that was observed during the first cycle [35–37]. After 100 cycles, the capacity retention of Co_3O_4/NC-1, Co_3O_4/NC-2, and Co_3O_4/NC-3 were 48.5%, 76.1%, and 42.4%, respectively. When

contrasted with Co_3O_4/NC-1 and Co_3O_4/NC-3, Co_3O_4/NC-2 has superior lithium storage performance. This can be mostly ascribed to the stable nanostructure of this material, which makes it easier to transport lithium ions. The specific capacity of Co_3O_4/NC-2 increased during the first few cycles. This was a phenomenon that could be attributed to the continuous activation of the electrode material that occurs during the process of charging and discharging the battery [38–40]. It is possible to draw the conclusion that the Co_3O_4/NC-2 composite possesses the highest electrochemical performance as a result. The favorable electrochemical performance of the Co_3O_4/NC-2 material can be primarily attributed to the synergistic effect between the highly conductive nitrogen-doped porous carbon covered on the surface of the Co_3O_4 nanoparticles and the highly conductive nitrogen nanoparticles. The Co_3O_4 nanoparticles make a significant amount of space available for the storage of Li^+, and the nitrogen-doped porous carbon speeds up the rate at which Li^+ can be inserted and removed from the material. The rate performance of Co_3O_4/NC-2 is illustrated in Fig. 3d under a variety of different current densities. When measured at a current density of 0.1 A g^{-1}, the specific capacity of Co_3O_4/NC-2 is found to be 1047 mAh g^{-1}. When the initial specific a capacity is decreased to 0.1 A g^{-1}, the specific capacity can still reach 1124.6 mAh g^{-1}. This represents an increase when compared to the initial specific a capacity and demonstrates excellent rate performance. This is as a result of the continuous activation of Co_3O_4/NC-2 under high current cycling, which gradually increases the number of active sites on the surface of the nanoparticles and accelerates the diffusion rate of Li^+, which ultimately results in an increase in specific capacity. In addition, the electrochemical impedance spectra (EIS) of Co_3O_4/NC-1, Co_3O_4/NC-2, and Co_3O_4/NC-3 were measured in the frequency range of 0.01 Hz-100 kHz (Fig. S8). The Nyquist plot consists of a semicircle in the high-frequency region, which corresponds to the charge transfer impedance of Li^+, and a slope in the low-frequency region, which corresponds to the diffusion impedance of Li^+ in the electrolyte [41]. It can be clearly seen that Co_3O_4/NC-2 has the smallest charge transfer resistance because Co_3O_4/NC-2 has a complete nanostructure and large specific surface area, which maximizes the accelerated Li^+ transport rate.

As can be seen in Fig. 4a, CV curves were measured at scan rates ranging from 0.2 to 1.0 mV s^{-1} with the objective of gaining a deeper understanding of the factors that led to the exceptional electrochemical performance of the Co_3O_4/NC-2 electrode material. It can be seen that the shapes of the CV curves are extremely similar at different scan rates, which is evidence that the Co_3O_4/NC-2 electrode possesses excellent cycle reversibility. The log(v) and log(i) curves that were obtained through calculation and fitting are depicted in Fig. 4b. i and v, in this equation, each stand for the peak current and the scan rate, respectively. The slope values obtained by fitting that are close to 0.5 indicate that the electrode reaction is controlled primarily by ion diffusion, whereas the slope values that are close to 1.0 indicate that the process is controlled predominantly by capacitance [42]. The slope values of 0.76 and 0.60 that were calculated can be seen in the figure. This demonstrates that the cycling process at the Co_3O_4/NC-2 electrode is primarily controlled by diffusion and that this control is the primary factor in the process. The diffusion-controlled process gives the electrode a high electrical capacity, which is beneficial for increasing the electrode's capacity to store lithium [43]. It can be seen from the capacitance and diffusion contribution ratios that were computed using Fig. 4c, d for a variety of scan rates that the contribution grows as the scan rate increases. Because of its distinctive nanoparticle structure, Co_3O_4/NC-2 provides an abundance of active sites for lithium ions, which contributes to the material's long-term cycling stability and excellent multiplicative performance. This is evidenced by the material's high capacitance contribution even when scanned at high rates. As can be seen in Fig. 4e, measurements using the galvanostatic intermittent titration technique (GITT) were carried out on the Co_3O_4/NC-2 electrode both before and after cycling in order to gain a deeper understanding of the transport process that occurs during the cycling of the system. Based on the previously reported diffusion equation [44], the calculated diffusion coefficients of Co_3O_4/NC-2 after 1 cycle were 2.3×10^{-12}–8.3×10^{-11} cm^2 s^{-1} and 3.2×10^{-11}–2.1×10^{-10} cm^2 s^{-1} after 50 cycles, as shown in Fig. 4f. During the cycling process, this phenomenon may be explained by the activation of the Co_3O_4/NC-2 electrode. The pore size in the nanoparticles gradually opens up, and the rate at which ions are transported increases, both of which contribute to an improvement in the electrochemical performance of the material. Furthermore, the morphological and structural information of the cycled Co_3O_4/NC-2 anode can be seen in the SEM image that can be found in Fig. S9. The nanoparticle structure of Co_3O_4/NC-2 can still be observed, despite the fact that it cannot be seen clearly due to the presence of conductive agents, binders, and electrolytes. This suggests that its structure remains stable even after repeated cycling.

Conclusion

In conclusion, a nanoparticle of Co_3O_4 that was successfully prepared was able to be uniformly encapsulated in a nitrogen-doped porous carbon matrix. This was accomplished by utilizing a high-temperature carbonization process on the precursor Co-MOF in conjunction with an in situ polymerization strategy. The one-of-a-kind nanostructure of this material offers a large number of active

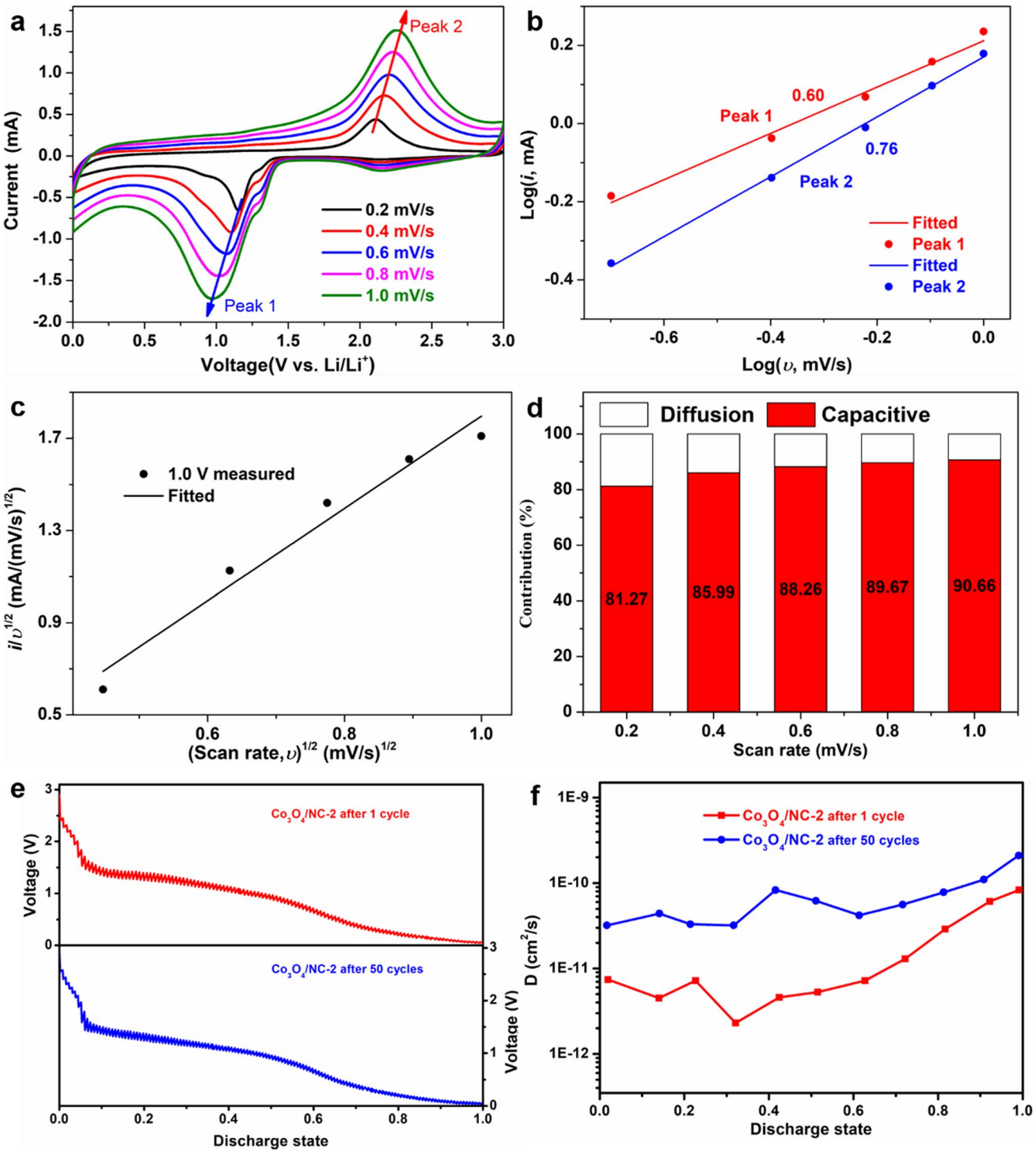

Fig. 4 **a** CV curves of Co_3O_4/NC-2 electrode at different scan rate ranging from 0.2 to 1.0 mV s^{-1}. **b** Log (*i*) versus log(*v*) plots. **c** $v^{1/2}$ versus $i/v^{1/2}$ plot used for calculating k_1 and k_2. **d** Contribution ratio of capacitive and diffusion-controlled behaviors at various scan rates. **e** GITT curves of Co_3O_4/NC-2 after 1 and 50 cycles; (**f**) the calculated Li chemical diffusion coefficients as a function of stoichiometry from GITT

sites for the exchange of lithium ions and electrons, and the increased stability of this material allows for significant volume expansion. As a result, the Co_3O_4/NC-2 electrode that was prepared demonstrated both high cycling performance (with a reversible specific capacity of 884.2 mAh g^{-1} after 100 cycles at 0.1 A g^{-1}) and high rate performance

(reversible specific capacity of 416.5 mAh g^{-1} at 5 A g^{-1}). According to this result, MOFs derived N-doped porous carbon-covered Co_3O_4 nanoparticle composites may open a new door for the construction of negative electrode materials for LIBs that have a higher energy density.

Supplementary Information The online version contains supplementary material available at https://doi.org/10.1007/s11581-022-04645-w.

Acknowledgements Z.P.Y. and X.D.C. contributed equally to this work. This work was supported by the National Natural Science Foundation of China (22065017, 22163003), China Postdoctoral Science Foundation (BX2021029, 2021M700353), the opening Foundation of State Key Laboratory of Organic-Inorganic Composites, Beijing University of Chemical Technology (oic-202201011), the Jiangxi Provincial Natural Science Foundation (20202BABL213012), Science Foundation from Education Department of Jiangxi Province (GJJ211801).

Declarations

Conflicts of interest The authors declare that they have no conflicts of interests.

References

1. Yang X, Zu H, Luo L, Zhang H, Li J, Yi X, Liu H, Wang F, Song J (2020) Synergistic tungsten oxide/N, S co-doped carbon nanofibers interlayer as anchor of polysulfides for high-performance lithium-sulfur batteries. J Alloys Compd 833:154969
2. Shi J, Xiao D, Ge M, Yu X, Chu Y, Huang X, Zhang X, Yin Y, Yang X, Guo Y, Gu L, Wan L (2018) High-capacity cathode material with high voltage for Li-Ion batteries. Adv Mater 30(9):1705575
3. Wang J, Jin D, Zhou R, Li X, Liu X, Shen C, Xie K, Li B, Kang F, Wei B (2016) Highly flexible graphene/Mn_3O_4 nanocomposite membrane as advanced anodes for Li-Ion batteries. ACS Nano 10(6):6227–6234
4. Yang H, Liu J, Wang X, Zhao C, Wang L, Wang Y, Xia Y, Liu T (2019) Positive surface pseudocapacitive behavior-induced fast and large Li-ion storage in mesoporous $LiMnPO_4$@C nanofibers. Chemsuschem 12(16):3817–3826
5. Guo L, Ru Q, Song X, Hu S, Mo Y (2015) Pineapple-shaped $ZnCo_2O_4$ microspheres as anode materials for lithium ion batteries with prominent rate performance. J Mater Chem 3(16):8683–8692
6. Rahman MA, Song G, Bhatt AI, Wong Y, Wen C (2016) Nanostructured silicon anodes for high-performance lithium-ion batteries. Adv Funct Mater 26(5):647–678
7. Feng Y, Bai C, Wu K, Dong H, Ke J, Huang X, Xiong D, He M (2020) Fluorine-doped porous SnO_2@C nanosheets as a high performance anode material for lithium ion batteries. J Alloys Compd 843:156085
8. Roy K, Li T, Ogale S, Robertson N (2021) Hybrid perovskite-like iodobismuthates as low-cost and stable anode materials for lithium-ion battery applications. J Mater Chem A 9(5):2689–2693
9. Shao J, Wan Z, Liu H, Zheng H, Gao T, Shen M, Qu Q, Zheng H (2014) Metal organic frameworks-derived Co_3O_4 hollow dodecahedrons with controllable interiors as outstanding anodes for Li storage. J Mater Chem 2(31):12194–12200
10. Wang L, Zheng Y, Wang X, Chen S, Xu F, Zou L, Wu J, Sun L, Li Z, Hou H, Song Y (2014) Nitrogen-doped porous carbon/Co_3O_4 nanocomposites as anode materials for lithium-ion batteries. ACS Appl Mater 6(10):7117–7125
11. Li J, Li J, Ding Z, Zhang X, Li Y, Lu T, Yao Y, Mai W, Pan L (2019) In-situ encapsulation of Ni_3S_2 nanoparticles into N-doped interconnected carbon networks for efficient lithium storage. Chem Eng J 378:122108
12. Wan L, Tang Y, Chen L, Wang K, Zhang J, Gao Y, Lee J, Lu T, Xu X, Li J, Zheng Y, Pan L (2021) In-situ construction of g-C_3N_4/Mo_2CT_x hybrid for superior lithium storage with significantly improved Coulombic efficiency and cycling stability. Chem Eng J 410:128349
13. Zhang Y, Li J, Gong Z, Xie J, Lu T, Pan L (2021) Nitrogen and sulfur co-doped vanadium carbide MXene for highly reversible lithium-ion storage. J Colloid Interf Sci 587:489–498
14. Zhang Y, Li J, Li H, Shi H, Gong Z, Lu T, Pan L (2022) Facile self-assembly of carbon-free vanadium sulfide nanosheet for stable and high-rate lithium-ion storage. J Colloid Interf Sci 607:145–152
15. Xu Y, Wang C, Niu P, Li Z, Wei L, Yao G, Zheng F, Chen Q (2021) Tuning the nitrogen-doping configuration in carbon materials via sulfur doping for ultrastable potassium ion storage. J Mater Chem A 9(29):16150–16159
16. Xu S, Cai L, Niu P, Li Z, Wei L, Yao G, Wang C, Zheng F, Chen Q (2021) The creation of extra storage capacity in nitrogen-doped porous carbon as high-stable potassium-ion battery anodes. Carbon 178:256–264
17. Xu Y, Chu K, Li Z, Xu S, Yao G, Niu P, Zheng F (2020) Porous CuO@C composite as high-performance anode materials for lithium-ion batteries. Dalton Trans 49(33):11597–11604
18. Chu K, Li Z, Xu S, Yao G, Xu Y, Niu P, Zheng F (2021) NiO nanocrystals encapsulated into a nitrogen-doped porous carbon matrix as highly stable Li-ion battery anodes. J Alloys Compd 854:157264
19. O'Keeffe M, Yaghi OM (2012) Deconstructing the crystal structures of metal-organic frameworks and related materials into their underlying nets. Chem Rev 112(2):675–702
20. Zhou H, Long J, Yaghi OM (2012) Introduction to metal-organic frameworks. Chem Rev 112(2):673–674
21. Deng H, Grunder S, Cordova KE, Valente C, Furukawa H, Hmadeh M, Gandara F, Whalley AC, Liu Z, Asahina S, Kazumori H, O'Keeffe M, Terasaki O, Stoddart JF, Yaghi OM (2012) Large-pore apertures in a series of metal-organic frameworks. Science 336(6084):1018–1023
22. Furukawa H, Cordova KE, O'Keeffe M, Yaghi OM (2013) The chemistry and applications of metal-organic frameworks. Science 341(6149):974
23. Huang M, Mi K, Zhang J, Liu H, Yu T, Yuan A, Kong Q, Xiong S (2017) MOF-derived bi-metal embedded N-doped carbon polyhedral nanocages with enhanced lithium storage. J Mater Chem 5(1):266–274
24. Wang Z, Zhang Z, Xia J, Wang W, Sun S, Liu L, Yang H (2018) Fe_2O_3@C core@shell nanotubes: Porous Fe_2O_3 nanotubes derived from MIL-88A as cores and carbon as shells for high power lithium ion batteries. J Alloys Compd 769:969–976
25. Wu Z, Ren W, Wen L, Gao L, Zhao J, Chen Z, Zhou G, Li F, Cheng H (2010) Graphene anchored with Co_3O_4 nanoparticles as anode of lithium ion batteries with enhanced reversible capacity and cyclic performance. ACS Nano 4(6):3187–3194
26. Hu Y, Yan C, Chen D, Lv C, Jiao Y, Chen G (2017) One-dimensional Co_3O_4 nanonet with enhanced rate performance for lithium ion batteries: carbonyl-β-cyclodextrin inducing and kinetic analysis. Chem Eng J 321:31–39
27. Zhai T, Wan L, Sun S, Chen Q, Sun J, Xia Q, Xia H (2017) Phosphate ion functionalized Co_3O_4 ultrathin nanosheets with greatly improved surface reactivity for high performance pseudocapacitors. Adv Mater 29(7):1604167

28. Dou Y, Xu J, Ruan B, Liu Q, Pan Y, Sun Z, Dou S (2016) Atomic layer-by-layer Co_3O_4 /graphene composite for high performance lithium-ion batteries. Adv Energy Mater 6(8):1501835
29. Yan C, Chen G, Zhou X, Sun J, Lv C (2016) Template-based engineering of carbon-doped Co_3O_4 hollow nanofibers as anode materials for lithium-ion batteries. Adv Funct Mater 26(9):1428–1436
30. Kang W, Zhang Y, Fan L, Zhang L, Dai F, Wang R, Sun D (2017) Metal–organic framework derived porous hollow Co_3O_4/N–C polyhedron composite with excellent energy storage capability. Mater Interfaces 9(12):10602–10609
31. Wang D, Yu Y, He H, Wang J, Zhou W, Abruna HD (2015) Template-Free synthesis of hollow-structured Co_3O_4 nanoparticles as high-performance anodes for lithium-ion batteries. ACS Nano 9(2):1775–1781
32. Hou Y, Li J, Wen Z, Cui S, Yuan C, Chen J (2015) Co_3O_4 nanoparticles embedded in nitrogen-doped porous carbon dodecahedrons with enhanced electrochemical properties for lithium storage and water splitting. Nano Energy 12:1–8
33. Tan Y, Gao Q, Yang C, Yang K, Tian W, Zhu L (2015) One-dimensional porous nanofibers of Co_3O_4 on the carbon matrix from human hair with superior lithium ion storage performance. Sci Rep 5:12382
34. Wang L, Zheng Y, Wang X, Chen S, Xu F, Zuo L, Wu J, Sun L, Li Z, Hou H, Song Y (2014) Nitrogen-Doped porous carbon/Co_3O_4 nanocomposites as anode materials for lithium-ion batteries. ACS Appl Mater Interfaces 6(10):7117–7125
35. Zhang D, Dai A, Fan B, Li Y, Shen K, Xiao T, Hou G, Cao H, Tao X, Tang Y (2020) Three-dimensional ordered macro/mesoporous Cu/Zn as a lithiophilic current collector for dendrite-free lithium metal anode. ACS Appl Mater Interfaces 12(28):31542–31551
36. Chen K, Pathak R, Gurung A, Adhamash EA, Bahrami B, He Q, Qiao H, Smirnova AL, Wu JJ, Qian Q, Zhou Y (2019) Flower-shaped lithium nitride as a protective layer via facile plasma activation for stable lithium metal anodes. Energy Storage Mater 18:389–396
37. Chen K, Pathak R, Gurung A, Reza KM, Ghimire N, Pokharel J, Baniya A, He W, Wu JJ, Qian Q, Zhou Y (2020) A copper-clad lithiophilic current collector for dendrite-free lithium metal anodes. J Mater Chem 8(4):1911–1919
38. Chang U, Lee JT, Yun J-M, Lee B, Lee SW, Joh H-I, Eom K, Fuller TF (2019) In situ self-formed nanosheet MoS_3/reduced graphene oxide material showing superior performance as a lithium-ion battery cathode. ACS Nano 13(2):1490–1498
39. Wu R, Wang D, Rui X, Liu B, Zhou K, Law AWK, Yan Q, Wei J, Chen Z (2015) In-Situ formation of hollow hybrids composed of cobalt sulfides embedded within porous carbon polyhedra/carbon nanotubes for high-performance lithium-ion batteries. Adv Mater 27(19):3038–3044
40. Cai D, Liu B, Wang D, Wang L, Liu Y, Qu B, Duan X, Li Q, Wang T (2016) Rational synthesis of metal-organic framework composites, hollow structures and their derived porous mixed metal oxide hollow structures. J Mater Chem 4(1):183–192
41. Xiao H, Xu L, Xiao Z, Huang H, Gan Y, Pan G, Tao X, Xia Y, Xia X, Zhang W (2019) Biological metabolism synthesis of metal oxides nanorods from bacteria as a biofactory toward high-performance lithium-ion battery anodes. Small 15(38):1902032
42. Chao D, Liang P, Chen Z, Bai L, Shen H, Liu X, Xia X, Zhao Y, Savilov SV, Lin J, Shen Z (2016) Pseudocapacitive Na-ion storage boosts high rate and areal capacity of self-branched 2D layered metal chalcogenide nanoarrays. ACS Nano 10(11):10211–10219
43. Duan M, Meng Y, Zhang H, Zhao G, Hu J, Ren G, Zhu F (2020) Facile synthesis of graphene-like carbon-coated Ni_3S_2 nanoparticles self-assembled on 3D dendritic nanostructure as high-performance anode materials of sodium-ion batteries. Ionics 26(9):4511–4522
44. Wang Y, Zhang Y, Li H, Peng Y, Li J, Wang J, Hwang B-J, Zhao J (2018) Realizing high reversible capacity: 3D intertwined CNT inherently conductive network for CuS as an anode for lithium ion batteries. Chem Eng J 332:49–56